A&A 668, A189 (2022)
https://doi.org/10.1051/0004-6361/202243989

Astronomy & Astrophysics
Special issue

Solar Orbiter First Results (Nominal Mission Phase)

Evolution of coronal hole solar wind in the inner heliosphere: Combined observations by Solar Orbiter and Parker Solar Probe

D. Perrone[1], S. Perri[2], R. Bruno[3], D. Stansby[4], R. D'Amicis[3], V. K. Jagarlamudi[3,5], R. Laker[6], S. Toledo-Redondo[7], J. E. Stawarz[6], D. Telloni[8], R. De Marco[3], C. J. Owen[4], J. M. Raines[9], A. Settino[2,10], B. Lavraud[11,12], M. Maksimovic[13], A. Vaivads[14], T. D. Phan[15], N. Fargette[12], P. Louarn[12], and I. Zouganelis[16]

[1] ASI – Italian Space Agency, Via del Politecnico snc, 00133 Rome, Italy
e-mail: denise.perrone@asi.it
[2] Dipartimento di Fisica, Università della Calabria, Rende, Italy
[3] National Institute for Astrophysics, Institute for Space Astrophysics and Planetology, Via del Fosso del Cavaliere 100, 00133 Rome, Italy
[4] Mullard Space Science Laboratory, Holmbury St Mary RH5 6NT, UK
[5] Johns Hopkins University Applied Physics Laboratory, Laurel, MD 20723, USA
[6] Department of Physics, Imperial College London, London SW7 2AZ, UK
[7] Department of Electromagnetism and Electronics, University of Murcia, Murcia, Spain
[8] National Institute for Astrophysics, Astrophysical Observatory of Torino, Via Osservatorio 20, 10025 Pino Torinese, Italy
[9] Department of Climate and Space Sciences and Engineering, University of Michigan, 2455 Hayward Street, Ann Arbor, MI 48109-2143, USA
[10] Space Research Institute, Austrian Academy of Sciences, Graz, Austria
[11] Laboratoire d'Astrophysique de Bordeaux, Univ. Bordeaux, CNRS, 33615 Pessac, France
[12] Institut de Recherche en Astrophysique et Planétologie, CNRS, UPS, CNES, 31028 Toulouse, France
[13] LESIA, Observatoire de Paris, Université PSL, CNRS, Sorbonne Université, Univ. Paris Diderot, Sorbonne Paris Cité, 5 Place Jules Janssen, 92195 Meudon, France
[14] KTH Royal Institute of Technology, SE-11428 Stockholm, Sweden
[15] Space Sciences Laboratory, University of California, Berkeley, CA 94720-7450, USA
[16] European Space Agency (ESA), European Space Astronomy Centre (ESAC), Camino Bajo del Castillo s/n, 28692 Villanueva de la Cañada, Madrid, Spain

Received 10 May 2022 / Accepted 29 July 2022

ABSTRACT

We study the radial evolution, from 0.1 AU to the Earth, of a homogeneous recurrent fast wind, coming from the same source on the Sun, by means of new measurements by both Solar Orbiter and Parker Solar Probe. With respect to previous radial studies, we extend, for the first time, the analysis of a recurrent fast stream at distances never reached prior to the Parker Solar Probe mission. Confirming previous findings, the observations show: (i) a decrease in the radial trend of the proton density that is slower than the one expected for a radially expanding plasma, due to the possible presence of a secondary beam in the velocity distribution function; (ii) a deviation for the magnetic field from the Parker prediction, supported by the strong Alfvénicity of the stream at all distances; and (iii) a slower decrease in the proton temperature with respect to the adiabatic prediction, suggesting the local presence of external heating mechanisms. Focusing on the radial evolution of the turbulence, from the inertial to the kinetic range along the turbulent cascade, we find that the slopes, in both frequency ranges, strongly depend on the different turbulence observed by the two spacecraft, namely a mostly parallel turbulence in the Parker Solar Probe data and a mostly perpendicular turbulence in the Solar Orbiter intervals. Moreover, we observe a decrease in the level of intermittency for the magnetic field during the expansion of the stream. Furthermore, we perform, for the first time, a statistical analysis of coherent structures around proton scales at 0.1 AU and we study how some of their statistical properties change from the Sun to the Earth. As expected, we find a higher occurrence of events in the Parker Solar Probe measurements than in the Solar Orbiter data, considering the ratio between the intervals length and the proton characteristic scales at the two radial distances. Finally, we complement this statistical analysis with two case studies of current sheets and vortex-like structures detected at the two radial distances, and we find that structures that belong to the same family have similar characteristics at different radial distances. This work provides an insight into the radial evolution of the turbulent character of solar wind plasma coming from coronal holes.

Key words. plasmas – turbulence – solar wind

1. Introduction

The solar wind, a weakly collisional plasma outflow from the Sun, is a highly variable medium whose global and local properties can change during its expansion in the heliosphere. Although some quantities, such as the ion abundances or the ionization state, remain almost steady during the solar wind trip from the Sun to the Earth, which helps to link in situ measurements with their coronal sources observed with remote sensing instruments, most of the plasma parameters strongly vary with the radial distance. Indeed, especially in fast solar wind, density decreases almost in the manner expected for a stationary radially

expanding plasma, while temperature does not, suggesting the presence of continuous heating mechanisms experienced by the plasma during its expansion (see e.g., Hellinger et al. 2011, 2013; Perrone et al. 2019a,b). A possible candidate for this local heating is turbulence in the solar wind (Coleman 1968; Bruno & Carbone 2013). The Sun injects energy in the form of large-wavelength fluctuations, such as Alfvén waves, into the heliosphere. These undergo a turbulent cascade that transfers energy toward shorter and shorter scales where fluctuations can be dissipated (Bruno & Carbone 2013; Verscharen et al. 2019). Generally, magnetic power spectra show a Kolmogorov-like power law at intermediate scales, the so-called inertial range (Kolmogorov 1941; Tu & Marsch 1995). Then, at smaller scales, where the ions are unmagnetized, the spectra become steeper (Leamon et al. 1998; Bale et al. 2005; Alexandrova et al. 2013), dissipation mechanisms play an important role, and the plasma dynamics is governed by kinetic properties (Marsch 2006; Servidio et al. 2015; Sorriso-Valvo et al. 2019). It has been observed that breaks in the magnetic power spectral density (PSD), which separate the large-scale range from the inertial range and the inertial range from the kinetic range, tend to be shifted toward higher frequencies as the radial distance decreases (D'Amicis et al. 2010; Bruno & Carbone 2013; Bruno & Trenchi 2014). Moreover, other properties of turbulence, such as Alfvénicity or intermittency, evolve during the expansion of the solar wind as well (see Bruno & Carbone 2013, and references therein).

The investigation of the radial evolution of the solar wind requires two or more radially aligned satellites at different heliospheric distances. This allows us to follow the same parcel of solar wind plasma during its radial expansion in the heliosphere. Examples of two-point alignments in the inner heliosphere occurred between the twin satellites Helios 1 and Helios 2 (Schwartz & Marsch 1983), and between Messenger and Wind (Bruno & Trenchi 2014; Bruno et al. 2014a; Telloni et al. 2015). Other examples can be found in the outer heliosphere between Wind and Ulysses (Bruno & Trenchi 2014), or ACE and Ulysses (D'Amicis et al. 2010). Very recently, thanks to the launch of Parker Solar Probe (PSP, Fox et al. 2016) and Solar Orbiter (Müller et al. 2020), a new two-point alignment has been studied, taking into account, for the first time, a completely unexplored environment very close to the Sun (Telloni et al. 2021). The authors were able to observe the evolution of the solar wind plasma from a highly Alfvénic and less developed turbulence state at about 0.1 AU toward a fully developed and intermittent turbulence state at 1 AU, thus confirming previous results.

Another approach for investigating the evolution of fast solar wind is to follow, at different radial distances, the plasma coming from the same coronal hole. In the past, Helios 2 observed a well-defined high-speed stream during three consecutive solar rotations, allowing us to study the radial evolution of turbulence (Bavassano et al. 1981, 1982a,b; He et al. 2013) and intermittency (Bruno et al. 2003, 2014b) between 0.31 and 0.89 AU. Recently, the large-scale expansion of fast solar wind and its thermodynamics have been investigated in the inner heliosphere by means of 16 intervals of unperturbed high-speed plasma from three different coronal holes, observed by both Helios 1 and Helios 2 at different radial distances and during a few consecutive solar rotations (Perrone et al. 2019a,b).

Although the alignment between spacecraft is the ideal method for such a study, statistical approaches can be used to enhance the amount of available data. These methods involve the use of different solar wind regimes that consider the bulk speed as a threshold to select fast or slow wind (Hellinger et al. 2011, 2013), or averages over 100 km s^{-1} wide speed intervals (see e.g., Marsch et al. 1982; Schwenn 1983). However, these choices based on the particle speed are too simplistic and they could potentially lead to erroneous conclusions, since they do not separate streams of different nature and origin. Indeed, recently, new characterizations discerning the solar wind by its origin have been adopted (e.g., Camporeale et al. 2017; Stansby et al. 2018).

In this paper, we study, for the first time, the radial evolution of a homogeneous fast stream of solar wind between 0.1 and 1 AU by using both measurements from Solar Orbiter, which observed the stream close to the Earth in two consecutive solar rotations, and data from PSP, which was connected to the same coronal hole during its sixth solar encounter. In particular, after looking at the global properties of this recurrent stream in Sect. 2, we focus on the radial evolution of large-scale properties, turbulence, the Alfvénic content, and intermittency in Sect. 3. Moreover, we investigate the nature of the turbulent magnetic fluctuations around proton scales during the expansion of the wind, and we statistically study the observed coherent events both close to the Sun and to the Earth. Finally, in Sect. 4 we summarize the results and discuss our conclusions.

2. Solar Orbiter and Parker Solar Probe observations

Solar Orbiter, launched in February 2020, is the first mission of the ESA's Cosmic Vision 2015−2025 program with a strong NASA participation. The aim of this solar mission is to investigate the Sun and the inner heliosphere, both in and out of the ecliptic. Although Solar Orbiter was in its cruise phase until November 2021, the in situ suite of instruments has been producing a large amount of science data (see e.g., D'Amicis et al. 2021a; Lavraud et al. 2021; Louarn et al. 2021; Owen et al. 2021).

In Fig. 1a we show the hourly averaged magnitude of the solar wind speed during the time interval between 15 July and 15 October 2020. Solar Orbiter crossed both slow and fast solar wind streams when it moved from its first perihelion to the Earth (Fig. 1b). This interval corresponds to the initial part of the ascending phase of the new solar cycle 25 and it is easy to recognize almost stable recurrent fast streams, such as those highlighted by the green shadows. Indeed, the two streams are observed with a delay of about 27 days, which corresponds to a solar rotation. Moreover, as shown in panel c, Solar Orbiter was at the same Carrington longitude during these two crossings of fast intervals, suggesting that the coronal hole that produces the first stream remains almost stable after one solar rotation, thus being the source also of the second fast interval.

To support this, in the top right panel of Fig. 1, we show a synoptic map constructed from daily images from 1 to 28 August taken at 193 Å by the Atmospheric Imaging Assembly (AIA, Lemen et al. 2012) telescope on board the Solar Dynamics Observatory (SDO, Pesnell et al. 2012). Dark areas in this map show coronal holes. Also shown with white lines are the predicted footpoints of solar wind observed by Solar Orbiter from 28 August to 30 August 2020. These are drawn using a common two-step backmapping procedure (Neugebauer et al. 1998). From the location of Solar Orbiter, solar wind is backmapped ballistically using the average solar wind speed listed in Table 1. Magnetic field lines are then traced through a potential field source surface (PFSS) model, computed with `pfsspy` (Stansby et al. 2020) using a Global Oscillations Network Group (GONG, Harvey et al. 1996) synoptic map observed on 28 August 2020 at 00:04:00 UT. Solar Orbiter was

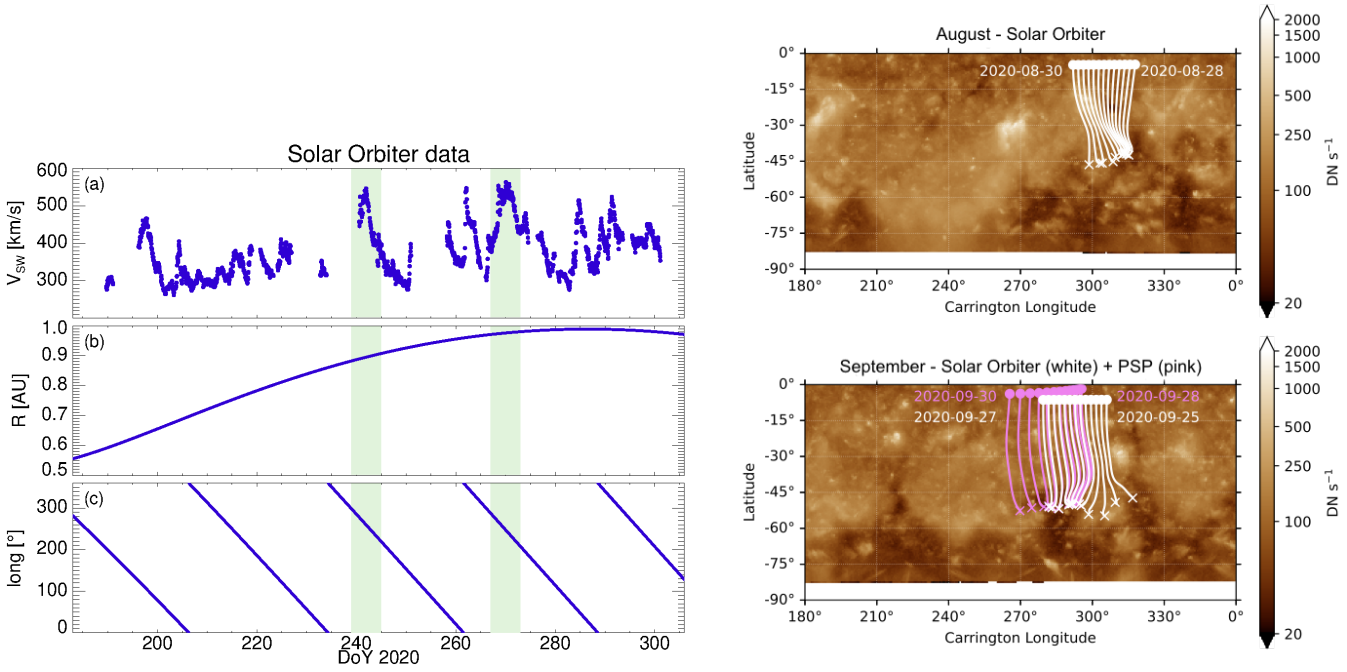

Fig. 1. Recurrent fast stream observed by Solar Orbiter and its source on the Sun. *Left*: hourly averaged Solar Orbiter data during the first months of the mission (between 15 July and 15 October 2020). *From top to bottom*: magnitude of the solar wind speed (*a*); distance from the Sun (*b*); and Carrington longitude (*c*), of the Solar Orbiter spacecraft. *Right*: partial synoptic maps from SDO/AIA 193 Å constructed from daily observations from 1 to 28 August (*top panel*) and 1 to 28 September (*bottom panel*). White and pink lines show magnetic field lines traced through a PFSS model from the source surface (dots) to the solar surface (crosses).

Table 1. Solar wind parameters (only protons are considered for ion moments and derived quantities), averaged over the selected recurrent stream observed by both Solar Orbiter and Parker Solar Probe.

Mission	Day	Start [UT]	End [UT]	R [AU]	V_{sw} [km s^{-1}]	n [cm^{-3}]	T [eV]	B [nT]
Parker Solar Probe	272	02:51:00	04:46:00	0.10	504 ± 45	462 ± 150	121 ± 18	210 ± 6
Solar Orbiter	241	01:53:00	06:45:00	0.89	476 ± 9	12.0 ± 0.8	15.0 ± 0.9	6.8 ± 0.2
Solar Orbiter	269	00:15:00	07:45:00	0.97	528 ± 14	6.6 ± 0.6	16 ± 2	5.2 ± 0.4
Mission				β	V_A [km s^{-1}]	λ [km]	ρ [km]	Ω_c [rad s^{-1}]
Parker Solar Probe				0.5 ± 0.2	234 ± 66	11 ± 3	7.4 ± 0.5	20.1 ± 0.5
Solar Orbiter				1.6 ± 0.2	41 ± 2	66 ± 2	87 ± 3	0.65 ± 0.02
Solar Orbiter				1.5 ± 0.2	48 ± 2	89 ± 4	101 ± 6	0.50 ± 0.04

Notes. The errors refer to the standard deviation evaluated in each interval.

connected to an equatorial coronal hole extension around 310° longitude at this time. During its sixth perihelion, in September 2020, at about 0.1 AU, PSP was connected to the same coronal hole, which produces the two recurrent fast streams observed by Solar Orbiter. Indeed, the bottom right panel of Fig. 1 displays the synoptic map a month later, constructed from daily AIA images from 1 to 28 September. Similar to the top panel, the predicted PSP (pink lines) and Solar Orbiter (white lines) connections are shown, using the GONG map observed on 28 September 2020 at 00:14:00 UT.

PSP allows us to have a privileged observational point of the plasma very close to the Sun, coming from the same source, observed close to the Earth by Solar Orbiter, and thus to investigate how it evolves during its expansion. We use both magnetic field and particle measurements by the two spacecraft. In particular, magnetic field data are from fluxgate magnetometers, while particle measurements are from top-hat electrostatic analyzers. For PSP we use MAG of the FIELDS suite (Bale et al. 2016) at 293 Hz and the Solar Probe ANalyzer for Ions (SPAN-I; Livi et al. 2021) of the SWEAP suite (Kasper et al. 2016) with a resolution of 3.5 s. The latter measures the three-dimensional ion distribution functions of the thermal corona and solar wind plasma, and, thanks to the time-of-flight capabilities, the ion composition. In our analysis, we focus on proton moments. For Solar Orbiter, we make use of MAG (Horbury et al. 2020a) for the magnetic field at 64 Hz for the interval in September, while at 8 Hz for the interval in August. Indeed, only one hour of data in burst mode is available for the considered stream in August, and therefore we use the normal mode. Finally, proton moments sampled at 4 s resolution from the Proton and Alpha particle Sensor (PAS) of the Solar Wind Analyser (SWA) suite (Owen et al. 2020) are used in this analysis.

Figure 2 shows plasma properties for the first twelve hours around the three encounters of the recurrent fast stream. Columns follow a chronological order; the first interval is observed by Solar Orbiter on 28 August at 0.89 AU (left column), then again Solar Orbiter was embedded in the same plasma on 25 September at 0.97 AU (middle column), and, finally, PSP observed the

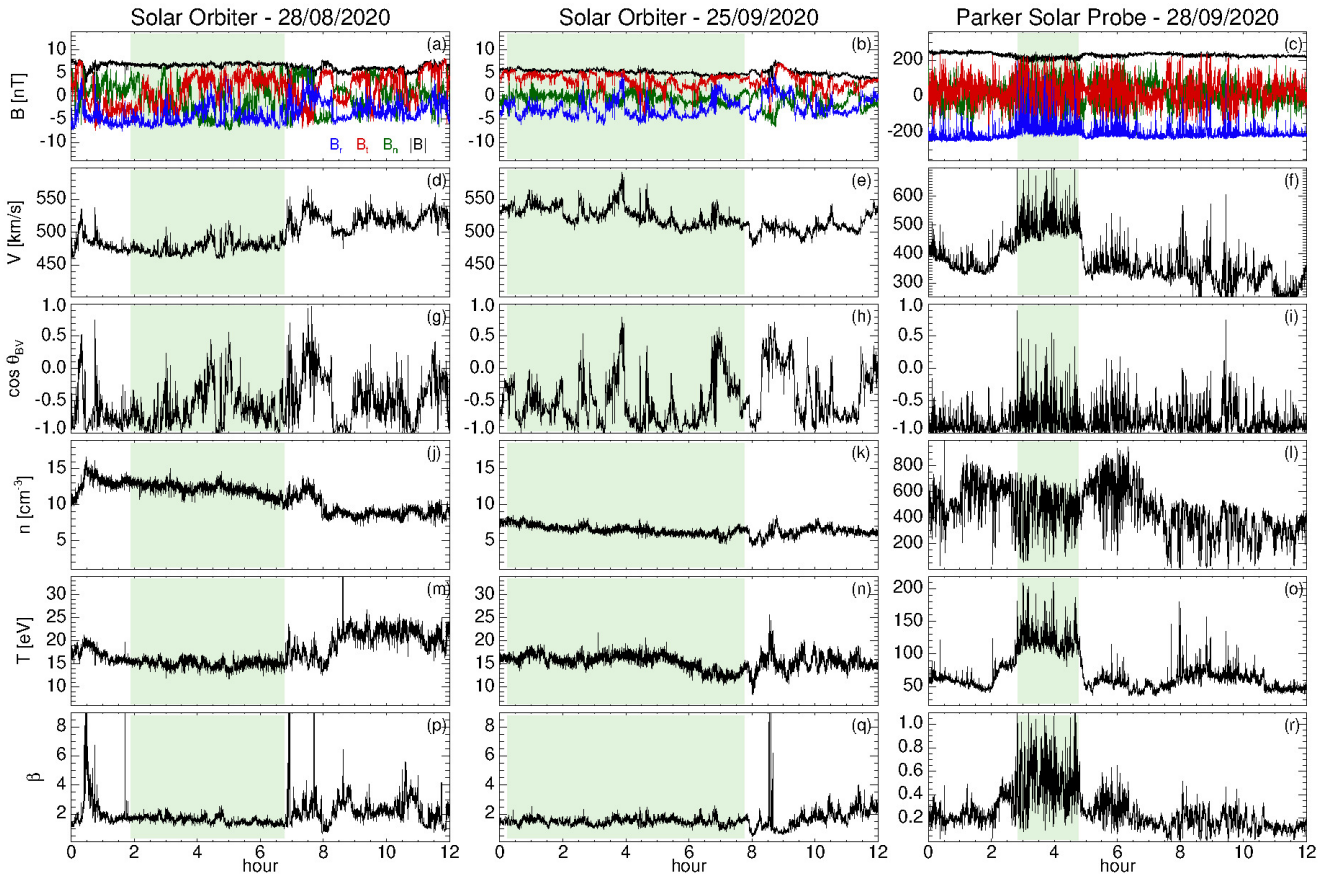

Fig. 2. Characteristics of the recurrent fast stream, highlighted by the green shadows, observed by Solar Orbiter on 28 August (*left column*) and on 25 September (*middle column*), and by PSP on 28 September (*right column*). *From top to bottom*: components in RTN (radial in blue, tangential in red, and normal in green) and magnitude (in black) of the magnetic field vector; magnitude of the solar wind speed; cosine of the angle between the magnetic and velocity field vectors; proton density; temperature; and plasma beta.

plasma coming from the same source on 28 September at 0.1 AU (right column). Each column, from top to bottom, shows: the three components in the radial tangential normal (RTN) reference frame (radial in blue, tangential in red, and normal in green) and magnitude (in black) of the magnetic field, B (panels a–c); the solar wind speed, V (panels d–f); the cosine of the angle between $\boldsymbol{B}$ and $\boldsymbol{V}$, $\cos\theta_{BV}$ (panels g–i); the proton density, n (panels j–l); temperature, T (panels m–o); and plasma beta, β (panels p–r). The periods used for the following analyses are highlighted by the green shadows. Table 1 displays the typical solar wind parameters, averaged within such intervals.

For Solar Orbiter measurements, shorter periods characterized by an almost constant plasma β (panels p and q) were selected for the analysis. Moreover, the magnitude of $\boldsymbol{B}$ (panels a and b) is nearly constant, as well as the temperature (panels m and n). Afterward, a magnetic discontinuity is detected (around 07:30:00 UT on 28 August and around 08:30:00 UT on 25 September), which corresponds to a change in the global behavior of the proton parameters (especially for n, T, and β). On the other hand, for PSP we consider the whole fast interval observed by the probe. Also, in this case the magnitude of $\boldsymbol{B}$ (panel c) is constant and the radial component B_r (blue line) is characterized by strong deflections, namely switchbacks (Bale et al. 2019; Dudok de Wit et al. 2020), associated with the presence of isolated intermittent velocity enhancements (Kasper et al. 2019; Horbury et al. 2020b). Indeed, panel f displays short and large amplitude speed enhancements, which are commonly observed in near-Sun fast streams (Horbury et al. 2018). For Solar Orbiter the presence of switchbacks and/or spikes are less clear, even if some magnetic field deflections and enhancements in the amplitude speed can be recognized. It is worth noting that, for PSP measurements, large fluctuations are also found for n, T, and β. Although they are related to the spikes in the speed, they could also be due to the instrumental noise of SPAN-I. In fact, ion velocity distribution function measurements by SPAN-I are limited by the heat shield, meaning that the full ion distribution is typically not in the field of view (FOV) of the instrument. SPAN-I data for the sixth encounter are much better than those during the previous ones, but the reader needs to be aware that the measures at the distance of 0.1 AU ($\sim$21.5 $R_\odot$) are still affected by this FOV problem (Kasper et al. 2016). Indeed, comparing the electron density from the plasma frequency (Moncuquet et al. 2020) with the proton density from SPAN-I measurements (not shown), we observe that the electron density has much smaller fluctuations, supporting the idea of a significant instrumental noise in SPAN-I data due to the FOV problem.

3. Radial evolution

Although we have solar wind measurements of this recurrent stream at only three different radial distances, we can still obtain the radial trend of the plasma properties and that of the magnetic field by fitting the averaged values reported in Table 1 with

Table 2. Fitting of the radial profile for some characteristic quantities of the recurrent fast stream, $f = f_0(R/1\,\mathrm{AU})^{\alpha}$.

	f_0	α
n [cm^{-3}]	8 ± 2	-1.8 ± 0.2
nV [10^3 cm^{-3} km s^{-1}]	3.9 ± 0.7	-1.8 ± 0.1
B [nT]	5.3 ± 0.4	-1.60 ± 0.05
$\lvert B_r \rvert$ [nT]	3.3 ± 0.4	-1.72 ± 0.09
$\lvert B_t \rvert$ [nT]	3.0 ± 0.4	-1.4 ± 0.1
T [10^5 K]	1.7 ± 0.1	-0.93 ± 0.04
β	1.58 ± 0.08	0.49 ± 0.04

a least-squares linear regression function in logarithmic space, $\log f = \alpha \log x + k$, with $x = R/R_0$ ($R_0 = 1$ AU) and $k = \log f_0$. Indeed, as reported by several previous studies (see e.g., Marsch et al. 1982; Hellinger et al. 2011; Perrone et al. 2019a), these quantities are linearly distributed with the radial distance in logarithmic space. All the results are summarized in Table 2, where the errors refer to the standard deviation (1-sigma uncertainty) estimates for the fit parameters.

We find that the radial dependence of the proton number density, n, is

$$n = (8 \pm 2)(R/R_0)^{(-1.8\pm0.2)}\,\mathrm{cm}^{-3}. \quad (1)$$

Although we expect to observe a decrease proportional to R^{-2}, typical of a radially expanding plasma, as found in Perrone et al. (2019a) for unperturbed coronal hole high-speed streams, our results are in agreement with the result found by Hellinger et al. (2011), $R^{-1.8}$, even if here the -2 index is recovered within the limit of the error. It is worth noting that, for both the PSP and Solar Orbiter data, we use direct integral moments of the proton distribution function (as also done by Hellinger et al. 2011, for Helios data), instead of fits where the contribution of a secondary proton beam can be neglected (as in the case of Perrone et al. 2019a). Thus, it seems that the presence of the proton beam could explain the differences between the two analyses. Moreover, the same radial trend is found for nV ($\propto R^{-1.8\pm0.1}$), namely an almost constant density flux. It is worth noticing that these results could be significantly influenced by the FOV problem of SPAN-I.

The radial evolution of the magnetic field magnitude is

$$B = (5.3 \pm 0.4)(R/R_0)^{(-1.60\pm0.05)}\,\mathrm{nT}, \quad (2)$$

in agreement with both the results found by Hellinger et al. (2011) and Perrone et al. (2019a). Then, if we look at the behavior of the radial and tangential components of the magnetic field, we find

$$|B_r| = (3.3 \pm 0.4)(R/R_0)^{(-1.72\pm0.09)}\,\mathrm{nT} \quad (3)$$

and

$$|B_t| = (3.0 \pm 0.4)(R/R_0)^{(-1.4\pm0.1)}\,\mathrm{nT}, \quad (4)$$

also in agreement with Perrone et al. (2019a), but in disagreement with the generally accepted structure of the interplanetary magnetic field. Indeed, according to the Parker model (Parker 1958), B_r and the transverse components should decrease as R^{-2} and R^{-1}, respectively (Mariani et al. 1979; Jokipii & Kóta 1989). The observed deviation could be explained by the strong Alfvénic character of these intervals (which is discussed later in the paper). As shown in Matteini et al. (2015), the large amplitude and nonlinearly polarized characteristics of the Alfvénic fluctuations tend to preferentially reduce the radial fluctuations with respect to the background state. Therefore, by considering the behavior of B_r due to the combination of a mean part and a fluctuating part, we could have the former, which radially varies in accordance with the Parker spiral, and the latter, which varies with a different scaling. Moreover, this behavior could be also influenced by turbulent processes during the expansion in the inner heliosphere (see e.g., Ragot 2006).

Proton temperature displays the following radial behavior:

$$T = (1.7 \pm 0.1) \times 10^5 (R/R_0)^{(-0.93\pm0.04)}\,\mathrm{K}. \quad (5)$$

As already shown in previous studies (Marsch et al. 1982; Hellinger et al. 2011; Perrone et al. 2019a), during the plasma expansion, the temperature decreases more slowly with respect to the adiabatic prediction, suggesting the presence of external heating mechanisms, which can locally play a non-negligible role. The index that we find is in good agreement with the results presented in Perrone et al. (2019a), while T decreases faster than in Hellinger et al. (2011). The difference could be due to the presence of interaction regions on the trailing edge of the high-speed streams in the data set used by Hellinger et al. (2011). These interaction regions represent an external source of heating (see Perrone et al. 2019a for more details).

Finally, the radial evolution of the proton plasma beta is

$$\beta = (1.58 \pm 0.08)(R/R_0)^{(0.49\pm0.04)}, \quad (6)$$

which increases from the Sun to the Earth, in agreement with the radial trends for the proton density, temperature, and magnetic field magnitude described above. This behavior suggests a faster decrease in the magnetic pressure with respect to the kinetic pressure during the radial expansion of the wind, in agreement with Perrone et al. (2019a).

3.1. Alfvénic content and energy distribution

Belcher & Davis (1971) showed, for the first time, the existence of Alfvénic correlations, in other words strong correlations between velocity and magnetic field fluctuations in the presence of near incompressibility. These periods mainly occur within fast streams, but even in Alfvénic slow intervals they are very common as well (see D'Amicis et al. 2021b, for a review on this topic). Alfvénic correlations are ubiquitous in the solar wind, and they become stronger and are shifted toward lower frequencies as the distance from the Sun decreases (Bruno et al. 1985; Roberts et al. 1987).

In order to better characterize the evolution of the homogeneous recurrent stream, in Fig. 3 we show the radial (panels a–c), tangential (panels d–f), and normal (panels g–i) components of the magnetic (black) and velocity (red) fields, normalized to the mean fields within each interval. Columns in Fig. 3 are organized by the distance from the Sun. Here, the velocity components by PSP in RTN coordinates are evaluated by using re-processed SPAN-I data, obtained from a systematic fitting with a bi-Maxwellian function of all the original proton distribution functions. The fitting routine is almost identical to the one described in Woodham et al. (2021) and has already been used for Helios particle data (Stansby 2017). A clear correlation in the components of the magnetic and velocity fields, and the almost constant values of the proton density and magnetic field magnitude (see Fig. 1), which suggest a low compressibility

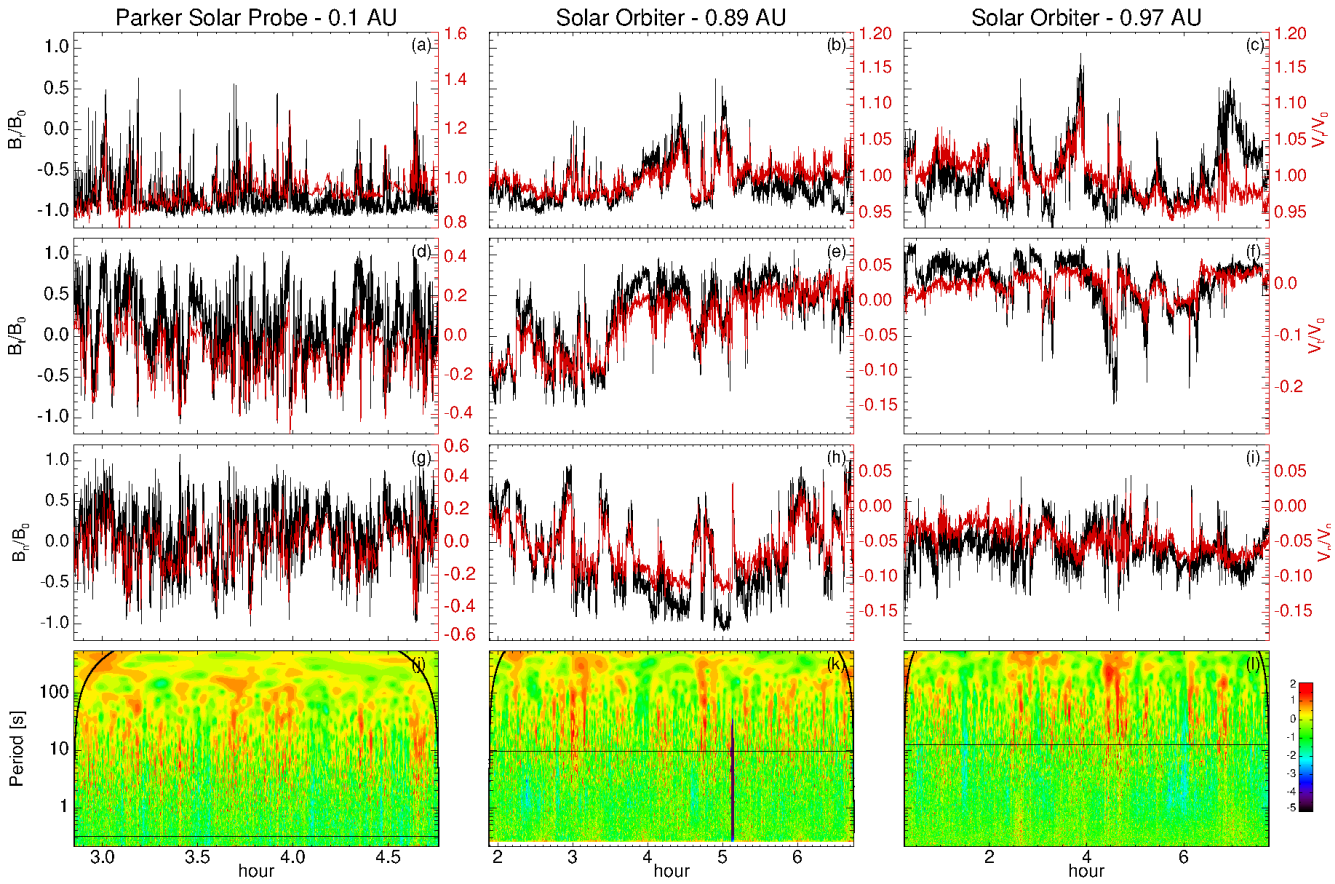

Fig. 3. Alfvénic and intermittency content for the recurrent fast stream at 0.1 AU (*left column*), 0.89 AU (*middle column*), and 0.97 AU (*right column*). *From top to bottom*: radial, tangential, and normal component of the magnetic (black) and velocity field (red), normalized to the mean fields; and logarithmic contour plots of the local intermittency measure (LIM) of the total magnetic field fluctuations, where horizontal lines denote the proton cyclotron timescale and curved lines, at each side of the plots, indicate the cone of influence.

(D'Amicis & Bruno 2015), confirm the strong Alfvénic character of these intervals. As mentioned in Sect. 2, PSP plasma data strongly fluctuate (e.g., a variation of $\sim$500 cm^{-3} in the proton density), maybe due to the instrumental noise of SPAN-I experiment. These fluctuations almost invalidate the evaluation of the usual parameters for the characterization of the Alfvénic content of the solar wind, such as the normalized cross helicity and the normalized residual energy. Therefore, we decided not to include these quantities in our analysis for the study of the radial evolution of the Alfvénicity.

In the bottom row of Fig. 3, we show the local intermittency measures (LIM, Farge 1992) for the total magnetic field fluctuations, $|\mathcal{W}_{\boldsymbol{B}}(\tau,t)|^2 = \sum_i |\mathcal{W}_i(\tau,t)|^2$ with $i = r,t,n$, defined as

$$I(\tau,t) = \frac{|\mathcal{W}_{\boldsymbol{B}}(\tau,t)|^2}{\langle |\mathcal{W}_{\boldsymbol{B}}(\tau,t)|^2 \rangle_t}, \tag{7}$$

where the brackets indicate a time average, and $\mathcal{W}_i(\tau,t)$ are the Morlet wavelet coefficients for different timescales τ and time t (Torrence & Compo 1998), namely

$$\mathcal{W}_i(\tau,t) = \sum_{j=0}^{N-1} B_i(t_j)\psi^*\left[\left(t_j - t\right)/\tau\right], \tag{8}$$

where ψ^* is the conjugate of the wavelet function. Horizontal black lines denote the averaged proton cyclotron timescale within each interval (values are very different between PSP and Solar Orbiter, as expected), while the curved lines, at each side of the plots, indicate the cone of influence, where the Morlet coefficients are affected by edge effects (Torrence & Compo 1998). At all radial distances, we find that the distribution of energy in time and timescales (not affected by edge effects) is not uniform, with the appearance of localized energetic events covering a certain range of timescales clearly recognizable by the red color (a black localized event for Solar Orbiter at 0.89 AU is due to a gap in magnetic data). This indicates the presence of coherent structures in these intervals forming at larger timescales and then transferring magnetic energy toward shorter timescales via a turbulent cascade process (Perrone et al. 2016, 2017; Lion et al. 2016). It is worth pointing out that the range of scales where energetic events are observed are not the same for PSP and Solar Orbiter. Indeed, the radial expansion from 0.1 AU to the Earth moves the characteristic scales toward larger timescales. We explore this point further in the next subsection.

3.2. Turbulence

Assuming that turbulence is in a stationary state and that small variations with heliographic latitude are negligible (see e.g., Bruno & Bavassano 1987), we analyze the radial dependence of the turbulent fluctuations in both the inertial and dissipative ranges of the turbulent cascade during the expansion of the recurrent fast stream. Figure 4 shows the total PSD (i.e., the trace of the spectral matrix) of the magnetic (a) and velocity (b) field

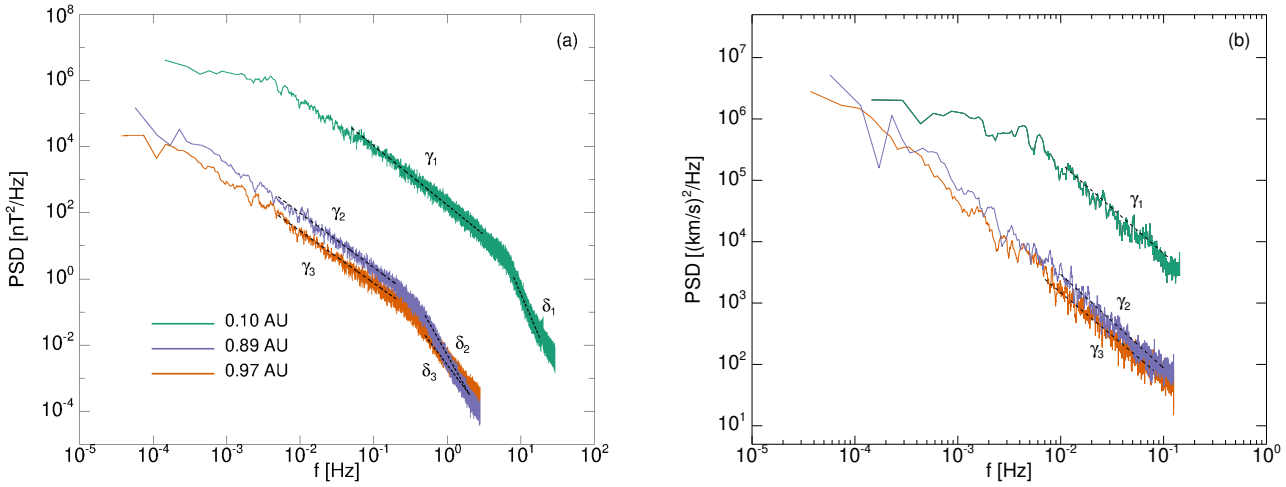

Fig. 4. Power spectral density (PSD) of the total magnetic (*panel a*) and velocity (*panel b*) field fluctuations for the interval observed by PSP (green) at 0.1 AU, and for the two intervals observed by Solar Orbiter at 0.89 AU (violet) and 0.97 AU (orange). Dotted black lines are the best power-law fits. The relevant slopes, indicated by γ and δ for the inertial and the dissipative ranges, are also reported.

Table 3. Radial evolution of the spectral index evaluated in both the inertial, γ, and dissipative, δ, range of the turbulent spectra in Fig. 4.

	Magnetic		Velocity
R [AU]	γ	δ	γ
0.10	-1.798 ± 0.006	-5.15 ± 0.01	-1.47 ± 0.05
0.89	-1.65 ± 0.01	-3.96 ± 0.01	-1.53 ± 0.03
0.97	-1.57 ± 0.01	-2.952 ± 0.009	-1.41 ± 0.02

Notes. The errors refer to the standard deviation (1-sigma uncertainty) estimates for the fit parameters.

fluctuations for the PSP data set (green) at 0.1 AU, and for the Solar Orbiter data sets at 0.89 AU (violet) and 0.97 AU (orange). As we expected, for both magnetic and velocity field fluctuations, the power level is higher for the stream close to the Sun and decreases as the radial distance increases. The dotted black lines in Fig. 4 indicate the best power-law fits at intermediate frequencies in the magnetohydrodynamics (MHD) range and at high frequencies in the dissipative or dispersion range. Both magnetic and velocity spectra show the characteristic behavior of the solar wind turbulent cascade, with a power-law trend between the Kolmogorov (Kolmogorov 1941) and the Kraichnan (Kraichnan 1965) scaling at the MHD frequencies for the magnetic field fluctuations (Bruno & Carbone 2013), and a spectral index closer to the Iroshnikov-Kraichnan scaling of $-3/2$ for the velocity field fluctuations (see e.g., Podesta et al. 2006, 2007; Salem et al. 2009). However, Roberts (2010) showed that the power spectrum of velocity fluctuations steepens with the radial distance toward a Kolmogorov scaling well past 1 AU, matching the magnetic spectrum behavior and the theoretical expectation of the Kolmogorov theory. Finally, Fig. 4 shows that, in the dissipative range, which can be resolved only for the magnetic field measurements, the spectral slopes become steeper. The spectral index values for the three radial distances, and for both magnetic and velocity field fluctuations, are summarized in Table 3.

For the velocity field fluctuations (panel b in Fig. 4), we observe that at all the radial distances covered by the observations, the velocity spectrum slope remains quite constant ($\gamma \sim -3/2$). This is in agreement with previous PSP observations described in Shi et al. (2021). On the other hand, for the magnetic field fluctuations (panel a in Fig. 4), we find that γ decreases (in absolute value) with the radial distance from -1.798 ± 0.006 at 0.1 AU to -1.57 ± 0.01 at 0.97 AU, which is in disagreement with the results presented by Chen et al. (2020). They found, in the inertial range (between 0.02 and 0.1 Hz), a transition between about $-3/2$ at 0.17 AU to about $-5/3$ at 0.6 AU, using magnetic field data over the first two PSP orbits, without any restrictions on solar wind conditions. Indeed, the orbits covered different source regions, but most of the solar wind observed was slow but Alfvénic, with fluctuations of large amplitude. Moreover, it is worth noting that we use a different range of frequency for the estimation of the spectral slope with respect to Chen et al. (2020). Indeed, we decided to use the whole well-defined range available for the inertial frequencies for each radial distance. At different radial distances, in fact, the characteristic frequencies are shifted toward low frequencies as the solar wind propagates from the Sun to the Earth, meaning that the choice of a fixed range forces the estimation of the spectral index in different parts of the power law. In an ideal case, this would not affect the result, but in real cases, not all the frequencies are resolved in the same way. Low frequencies are strongly affected by the length of the considered interval, while high frequencies depend on the time resolution of the considered measurements. However, the disagreement remains if we also consider the same fixed range used in Chen et al. (2020).

Looking in greater detail at the properties of the velocity and magnetic field fluctuations, discrepancies in the results from the spectral analysis seem to be ascribed to different turbulence properties observed by the spacecraft. Indeed, by considering the cosine of the angle between the total magnetic and velocity field vectors for the selected intervals (see panels g–i in Fig. 2), we find that in the PSP data, $\cos\theta_{BV}$ is closer to -1 (i.e., antiparallel magnetic and velocity field vector) than in the Solar Orbiter data. Therefore, PSP samples a more parallel turbulence, while Solar Orbiter looks at a more perpendicular turbulence. This is reflected in the values of the spectral indices, in the Solar Orbiter samples closer to a Kolmogorov and/or Kraichnan power-law, and in the PSP data set closer to -2. However, it is worth noticing that, although the angle θ_{BV} for PSP indicates that we sample the solar wind mainly parallel to the local field, γ_1 does not have exactly the expected value of -2 predicted by the critical balance theory (GS95, Goldreich & Sridhar 1995). As shown by

Horbury et al. (2008), the spectral index for quasi parallel sampling quickly departs from −2 for angles larger than about 10° (see also von Papen & Saur 2015). In our case the angle θ_{BV}, averaged over all of the PSP interval, is larger than 10°. However, for the sake of completeness, we have to add that the deviation from −2 can be explained by other reasons, such as the applicability of the GS95 theory to strong turbulence, in which opposite Alfvénic modes have the same amplitude and cross helicity is close to zero, or the presence of strong intermittency, which can have a steepening effect on the spectrum.

Moving to higher frequencies, we observe the development of a dissipative range as a steeper power-law appears in the PSD (Sahraoui et al. 2009). From Fig. 4a it is clear that the spectral break, identified around proton frequencies, moves toward lower and lower frequencies as the radial distance increases (Bruno & Trenchi 2014). Moreover, we observe during the expansion that δ decreases (in absolute value) from −5.15±0.01 to −2.952±0.009, in agreement with the results presented by Duan et al. (2020). This interesting feature can again be explained by the anisotropy of the magnetic field, which tends to be mainly aligned to the radial direction at 0.1 AU (see right panel in Fig. 2) and more oblique to it toward 1 AU. The magnetic turbulent cascade is indeed mainly dominated by the k-vectors perpendicular to the mean field also at sub-ion scales (Sahraoui et al. 2010), which are sampled in the Solar Orbiter data. On the other hand, in the Alfvénic stream observed by PSP, the radial direction is almost aligned with the mean field direction, so that the cascade observed is mainly due to $k_{\|}$ (assuming the Taylor, frozen-in, hypothesis). This further suggests the dominance of quasi-perpendicular modes in the kinetic range in Alfvénic turbulence.

3.3. Intermittency

We now focus our analysis on the two fast intervals observed in September by PSP and Solar Orbiter, namely the interval closest to the Sun and the interval closest to the Earth. Indeed, both intervals have magnetic field data with the highest temporal resolution, which is required for the analysis of small-scale coherent structures, responsible for intermittency and described in detail in Sect. 3.4.

Here we perform a standard analysis, starting from the computation of the magnetic field increments, namely

$$\delta B_i(\tau, t) = B_i(t + \tau) - B_i(t), \tag{9}$$

where i runs over the vector components and τ is a time lag and scale. Then, we use the standardized variables for the magnetic field increments by computing the mean value (μ_i) at each timescale and the standard deviation of the increments, σ_i. This allows us to directly compare the probability density functions (PDFs) of the standardized variables of the increments at different timescales. PDFs are displayed in Fig. 5 for the recurrent fast stream at 0.1 AU (left column) and 0.97 AU (right column). From top to bottom, we show the PDFs of the radial, tangential, and normal components of the magnetic field increments, for three different timescales, τ (see the figure legend). Such timescales cover the whole inertial range. Different τ were used for PSP and Solar Orbiter, since the inertial range shifts from higher (smaller) to lower (larger) frequencies (timescales), as clearly displayed in Fig. 4a from 0.1 to 0.97 AU. Not surprisingly, the magnetic fluctuations are non-Gaussian and the departure from Gaussianity increases toward smaller scales (from blue to black lines) (Frisch 1995). For reference, the best Gaussian fit, for each magnetic component, is plotted in each panel as a black dashed line. We observe the presence of significant non-Gaussian tails in each component of the magnetic field fluctuations due to the presence of coherent magnetic events in which magnetic energy tends to clusterize (see Sect. 3.4). Moreover, Fig. 5 suggests that higher tails are recovered in the radial direction.

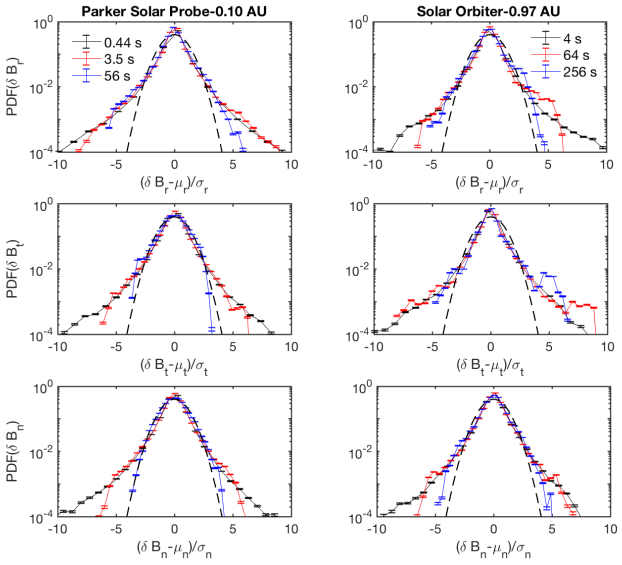

Fig. 5. Overview of the intermittency analysis performed for the recurrent fast stream at 0.1 AU (*left column*), and 0.97 AU (*right column*). *From top to bottom*: PDFs of the magnetic field increments at three different timescales τ (see legends) for the radial (*top row*), tangential (*middle row*), and normal (*bottom row*) components. For reference, the best Gaussian fit for each magnetic component is also reported (dashed black line). The PDFs have been computed over the standardized increments (see text for details).

To quantify the observed intermittency, we compute the fourth-order moment of the distribution of the increments, the so-called kurtosis, as (Frisch 1995):

$$K_i(\tau) = \frac{\langle \delta B_i(t,\tau) \rangle_{t_*}^4}{(\langle \delta B_i(t,\tau) \rangle_{t_*}^2)^2}, \tag{10}$$

where $\langle \cdots \rangle_{t_*}$ represents a time average over a given interval of length t_*. $K(\tau)$ essentially gives a measure of the degree of deviation of the distribution of the magnetic field increments from a Gaussian distribution, for which $K(\tau) = 3$ (dashed line in Fig. 6). We also compute the errors for each timescale as the dispersion calculated over a running window through the time series of about 240 s (70 000 data points) for PSP and 300 s (20 000 data points) for Solar Orbiter. The timescales in Fig. 6 have been rescaled to the one corresponding to the minimum wavenumber of the proton cyclotron damping resonance for outward propagating Alfvén waves and slab configuration, namely $k_{\rm res} = \Omega_{\rm c}/(V_{\rm A} + v_{\rm th})$, $\Omega_{\rm c}$ being the proton cyclotron frequency, and assuming that protons travel at the plasma thermal speed $v_{\rm th}$ and that the damping starts at $\omega_{\rm res} = kV_{\rm A}$ (Leamon et al. 1998). It has indeed been shown in Bruno et al. (2014a) that the ion scale spectral break in the PSD of the magnetic field fluctuations scales radially as the wavenumber corresponding to the linear resonance condition for proton cyclotron damping. We rescaled the time lags since, as deduced from Fig. 4a, the characteristic frequencies, and then the extension of the inertial range, strongly depend on the radial distance. Indeed, if we perform the same rescaling for the frequencies in Fig. 4a for both PSP and Solar

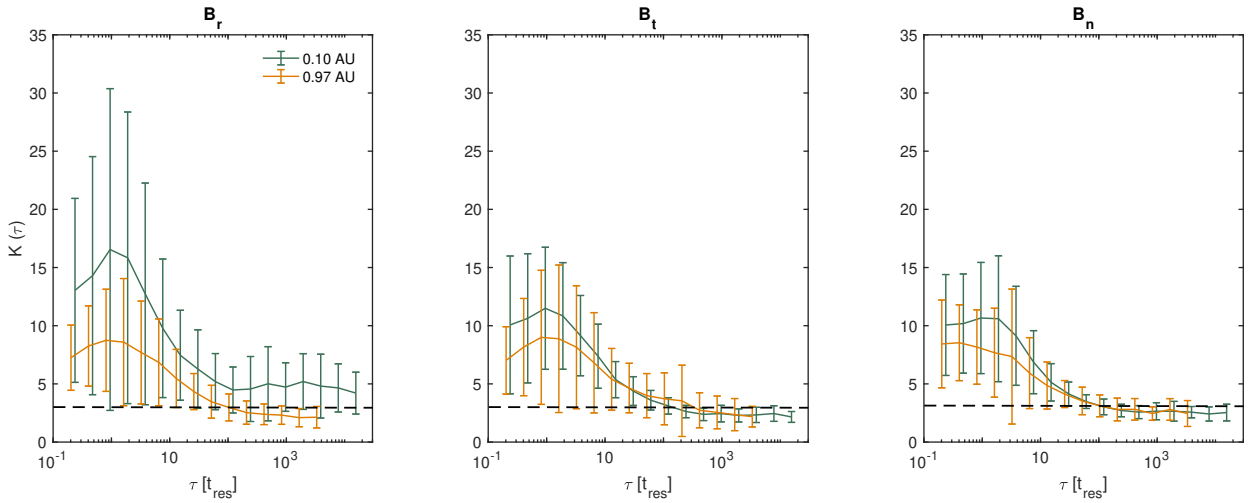

Fig. 6. Kurtosis as a function of the time lag τ rescaled to the proton cyclotron resonance timescale $t_{\rm res} = 1/f_{\rm res} = 2\pi(V_{\rm A} + v_{\rm th})/(\Omega_{\rm c} V_{\rm sw})$ in lin-log axis. It is important to notice that the minimum timescale at which the kurtosis has been plotted corresponds to the highest frequency shown in the PSD in Fig. 4a. Smaller timescales indeed are highly affected by instrumental noise. Error bars are also displayed (see text for further details). The horizontal dashed line indicates the value of the kurtosis for a Gaussian distribution of the magnetic field increments, i.e., $K(\tau) = 3$.

Orbiter data, namely using the proton cyclotron resonance frequency, $f_{\rm res}$, the characteristic ranges of the turbulent cascade are almost located at the same normalized frequencies (not shown).

It has been observed that in solar wind turbulence, $K_i(\tau)$ largely deviates from its Gaussian value at short timescales τ (Marsch & Tu 1997; Sorriso-Valvo et al. 1999; Bruno & Carbone 2013) in the inertial range, since the plasma becomes more nonhomogeneous as τ becomes shorter. On the other hand, high-resolution spacecraft measurements have allowed us to calculate the degree of intermittency at sub-ion timescales where kinetic effects come into play. While from fluid-like toward proton timescales the kurtosis tends to increase as τ decreases, within the sub-ion range kurtosis starts flattening (Kiyani et al. 2009; Wu et al. 2013; Yordanova et al. 2015), with $K(\tau) > 3$, but without a significant increase as τ decreases. This behavior can be ascribed to a reduction of coherent structures toward electron timescales, probably due to a stronger plasma wave activity (Wu et al. 2013). Such properties have also been found in our intervals at the two different radial distances. Indeed, Fig. 6 shows a tendency toward a saturation of (and a slight decrease in) the fourth-order moment of the magnetic field increments for all the three vector components and typically for $\tau < t_{\rm res}$. Figure 6 confirms that the PSP interval tends to have a larger kurtosis at proton and sub-proton scales. In order to highlight the possible contribution of the magnetic switchbacks to the high kurtosis in the B_r component of the PSP data, we selected these structures using a technique shown in Dudok de Wit et al. (2020), where α is the angle between the pointwise magnetic field and the mean field (computed over the whole ∼2 h interval) directions in the PSP data set. We then defined a quantity $z = (1 - \cos(\alpha))/2$, which measures the folding of the magnetic field, and picked all those periods during which $z \geq 0.5$ (i.e., rotations of the field greater than 90°). We then removed such periods that can be identified as switchbacks, interpolated the data (using a methodology similar to Bruno et al. 2001) and recalculated the kurtosis. The new kurtosis for the PSP data (not shown) is substantially reduced along the radial direction and no big differences can be observed among the three magnetic field components. Thus, the higher kurtosis found in the B_r component of the PSP data can be ascribed to the presence of magnetic switchbacks.

3.4. Coherent structures

In order to characterize the intermittency observed in the two fast streams in Sect. 3.3, we bandpass filtered the magnetic fluctuations around the proton timescales, applying a technique based on the wavelet transform (Torrence & Compo 1998; He et al. 2012; Perrone et al. 2016, 2017, 2020). Once again, we selected different ranges of frequencies for the two radial distances, namely $f \in [1, 10]$ Hz at 0.1 AU and $f \in [0.1, 1]$ Hz at 0.97 AU, which correspond to proton timescales in the two data sets. Magnetic fluctuations are then defined as

$$\delta b_i(t) = \frac{\delta j \delta t^{1/2}}{C_\delta \psi_0(0)} \sum_{j=j_1}^{j_2} \frac{\mathcal{R}\left[\mathcal{W}_i(\tau_j, t)\right]}{\tau_j^{1/2}}, \tag{11}$$

where $\mathcal{R}$ refers to the real-part function, j is the scale index, and δj is a constant scale step; $\psi_0(0) = \pi^{1/4}$ and $C_\delta = 0.776$, the latter derived from the reconstruction of a δ function using the Morlet wavelet (Torrence & Compo 1998). Finally, $\tau(j_1) = 0.1$ s and $\tau(j_2) = 1$ s for PSP, and $\tau(j_1) = 1$ s and $\tau(j_2) = 10$ s for Solar Orbiter (with $\tau = 1/f$). The PDFs of the magnetic field fluctuations around proton scales (not shown here) reveal the presence of significant non-Gaussian tails, due to the presence of extreme events (Perrone et al. 2016, 2017, 2020). These extreme events have been studied by selecting only the fluctuations that exceed three standard deviations from the corresponding Gaussian distribution, which includes 99.7% of the Gaussian contribution. Using an automated method, more than a thousand intermittent events have been detected in both intervals, thus supporting a statistical study of their properties. It is worth noting that we found almost double the number of events at 0.1 AU than at 0.97 AU. However, we need to consider that the time length of the two intervals is different. Indeed, if we use a normalized length to their characteristic proton cyclotron resonance timescale, or to the inverse of the Larmor radius or inertial length frequencies, we find that the ratio between the PSP and Solar Orbiter normalized length is between two and three. Thus, we should expect a larger number of coherent events in the PSP interval. Indeed, the ratio between the number of structures revealed by PSP and Solar Orbiter is ∼1.7.

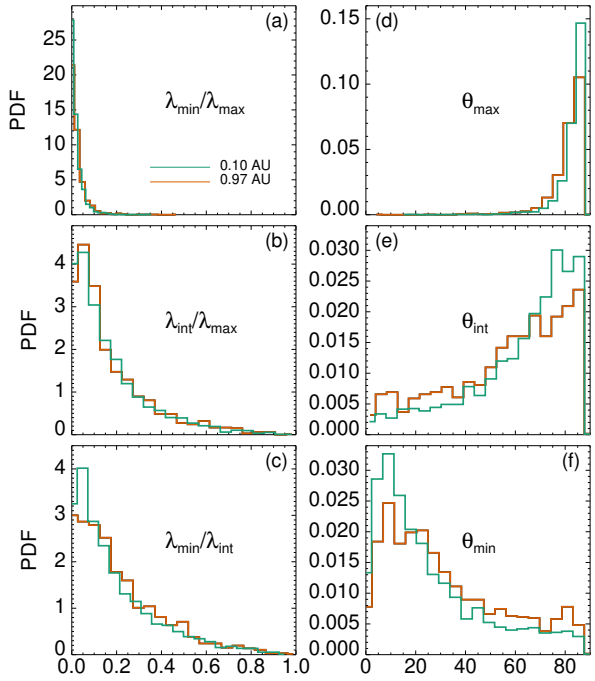

Fig. 7. Statistical analysis of the observed coherent events in the minimum variance reference frame for the stream at 0.1 AU (green), and at 0.97 AU (orange). *Left panels*: PDFs for the minimum (*a*) and intermediate (*b*) eigenvalues normalized to the maximum eigenvalue, and for $\lambda_{min}/\lambda_{int}$ (*c*). *Right panels*: PDFs of the angles between the maximum (*d*), intermediate (*e*), and minimum (*f*) variance directions and the local magnetic field.

We perform a minimum variance analysis (Sonnerup & Scheible 1998) around each selected peak in magnetic energy, corresponding to magnetic fluctuations well-localized in time (as shown in the bottom panels of Fig. 3) and with a regular profile in a range, $\Delta t'$, namely the width of the event, defined as the time interval between two minima of energy that contains the selected maximum over the threshold. On the other hand, we define the characteristic temporal scale of the event, Δt ($<\Delta t'$), as the width at half-height of the maximum (Perrone et al. 2016). Figure 7 displays the results in the minimum variance reference frame (MVRF) for the intermittent events found at 0.1 (green) and 0.97 AU (orange). In particular, the left column shows the PDFs of the eigenvalues, λ, while the right column displays the PDFs of the orientation of the eigenvectors, θ, with respect to the local magnetic field, $\boldsymbol{b}_0$, also averaged within the structure, and thus in $\Delta t'$.

We find that, in both intervals, most of the events are described by fluctuations with $\lambda_{min} \ll \lambda_{int} \ll \lambda_{max}$. However, we also recover the presence of fluctuations with $\lambda_{min} \ll \lambda_{int} \lesssim \lambda_{max}$. Then, the minimum variance direction is well defined, even if a degeneracy $\lambda_{min} \sim \lambda_{int}$ exists for very few events. Some differences between the two intervals can be found in the distributions of θ. Although, the direction of maximum variation, θ_{max}, is perpendicular to $\boldsymbol{b}_0$ in both the streams, suggesting the absence of compressive events, we find slightly different distributions for θ_{int} and θ_{min} at the two different radial distances. Indeed, close to the Sun, θ_{int} is peaked around 90° and θ_{min} is almost parallel to $\boldsymbol{b}_0$, while close to the Earth, θ_{int} and θ_{min} are less peaked and show higher tails, going toward a more uniform distribution. The latter is in agreement with the observations in fast wind at 1 AU with Cluster measurements (Perrone et al. 2017). Indeed, these results suggest that, as the radial distance increases from 0.1 to 0.97 AU, some mechanisms could generate a mix-up of the intermediate and minimum directions, and thus all possible angles can be covered.

Furthermore, in Fig. 8 we show the PDFs of the plasma β (panel a), of the θ_{BV} (panel b), and of the local magnetic compressibility, $\zeta_{\parallel}$ (panel c). β and θ_{BV} are the averaged values within $\Delta t'$ for each intermittent event, while $\zeta_{\parallel}$ is defined as (Perrone et al. 2016)

$$\zeta_{\parallel} = \sqrt{\frac{\max\left(\delta b_{\parallel}^2\right)}{\max\left(\delta b_{\perp 1}^2 + \delta b_{\perp 2}^2\right)}}, \tag{12}$$

where parallel and perpendicular directions are estimated with respect to $\boldsymbol{b}_0$ and the maximum of the magnetic components is evaluated within $\Delta t'$.

Panel a shows that the distributions of the proton plasma beta within the intermittent events, both at 0.1 AU (green) and 0.97 AU (orange), are peaked at the values reported in Table 1 and are in agreement with the β radial dependence. Moreover, although the two distributions have the same variance, they are slightly asymmetrical, with a negative skewness for PSP measurements and a positive skewness for Solar Orbiter observations. On the other hand, the distributions of θ_{BV} display a different behavior. At 0.1 AU we observe a peak at $20° < \theta_{BV} < 45°$, while a more uniform distribution between $\theta_{BV} \sim 30°$ and ~90° is found at 0.97 AU. Finally, in the two data sets, the distributions of $\zeta_{\parallel}$ show a peak around 0.2, meaning that the recovered intermittent events are characterized by a low magnetic compressibility, in agreement with previous observations in fast solar wind intervals, both in the inner heliosphere (Bavassano et al. 1982a) and close to the Earth (Perrone et al. 2017). It is worth pointing out that a slightly higher compressibility is found in Solar Orbiter measurements, where a higher tail and a small shift of the peak toward larger values of $\zeta_{\parallel}$ are recovered with respect to the one in the PSP data. This result could be related to the behavior observed for θ_{BV} and it will be investigated in a future work.

Looking into the details of each intermittent structure, we find that these events can be described mostly as currents sheets and vortex-like structures. A few examples of wave packets have also been identified. In Figs. 9 and 10, we compare examples of current sheets and vortex-like structures, respectively, observed at 0.1 (left columns) and 0.97 AU (right columns). In particular, we show the magnetic field fluctuations, as defined in Eq. (11), in both the MVRF (top rows), and in the local magnetic field reference frame (bottom rows) where $\boldsymbol{b}_0$ is along the z-direction ($\boldsymbol{e}_z = \boldsymbol{e}_b$), x is perpendicular to $\boldsymbol{b}_0$ in the plane spanned by it and the radial direction ($\boldsymbol{e}_x = \boldsymbol{e}_b \times \boldsymbol{e}_r$), and y closes the right-hand reference frame ($\boldsymbol{e}_y = \boldsymbol{e}_b \times \boldsymbol{e}_x$). In order not to be biased by the different radial distances, namely the fact that the magnetic field amplitude close to the Sun is stronger than the one observed close to the Earth, we decide to show the magnetic fluctuations normalized to the local mean magnetic field, b_0. Finally, the vertical dashed lines mark the width of the events, $\Delta t'$, where the analyses have been performed. It is worth noting that $\Delta t'$ for the structures observed by PSP is much smaller than the one for the structures observed by Solar Orbiter. This is not surprising since the proton characteristic scales, which are the focus of our analysis on coherent structures, are shifted toward larger timescales (or toward lower frequencies) as the solar wind flows from the Sun to the Earth.

Figure 9 shows two examples of a one-dimensional (i.e., a linearly polarized) structure, which can be identified as a current sheet. In both the events, the magnetic component that changes

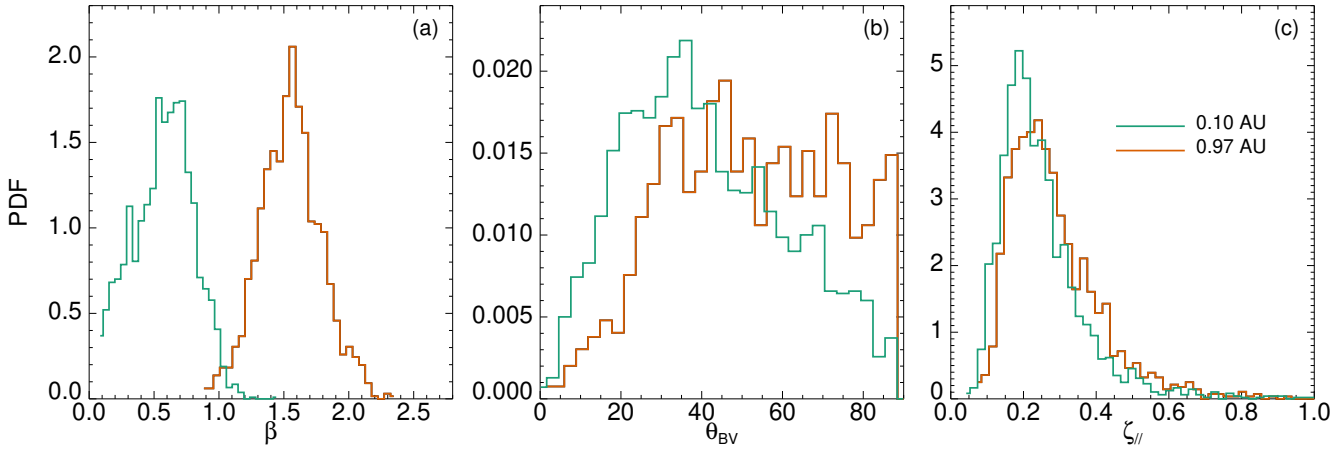

Fig. 8. PDFs of β (a), θ_{BV} (b), and $\zeta_{\parallel}$ (c), for the observed coherent events in the stream at 0.1 AU (green), and at 0.97 AU (orange).

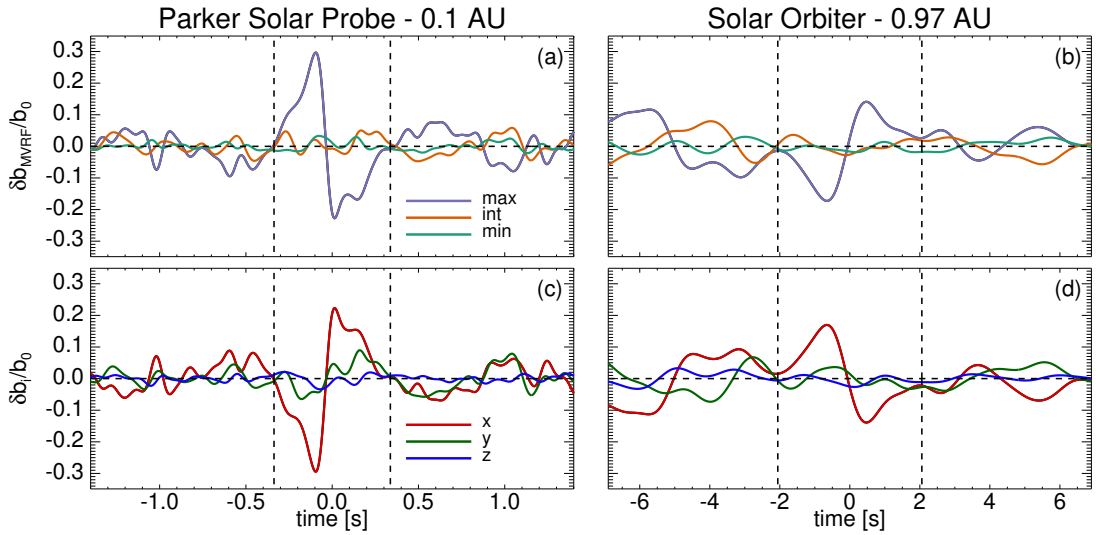

Fig. 9. Example of two current sheets observed at 0.1 AU (*left column*), and at 0.97 AU (*right column*), centered at 02:57:24.99 UT on 28 September and at 02:29:42.04 UT on 25 September, respectively. *Top row*: components of the magnetic field fluctuations, defined in Eq. (11), in the minimum variance reference frame. *Bottom row*: components of the magnetic field fluctuations in the local magnetic field reference frame, where $\boldsymbol{b}_0$ is along the z-direction. Magnetic fluctuations are normalized to the local mean magnetic field strength, b_0. The vertical dashed black lines mark the extension of the events, $\Delta t'$.

sign is δb_x (panels c and d), perpendicular to $\boldsymbol{b}_0$, and it exhibits a larger amplitude at 0.1 AU than at 0.97 AU. The other two components display very small fluctuations at both distances. To quantitatively compare these structures, we discuss the results of the minimum variance analysis. In both cases, $\lambda_{\rm max} \gg \lambda_{\rm int}, \lambda_{\rm min}$ and the direction of maximum variation is perpendicular to $\boldsymbol{b}_0$, with $\theta_{\rm max} \sim 89°$ and $88°$ at 0.1 and 0.97 AU, respectively. Finally, assuming that these structures are convected by the wind, we can estimate their characteristic width, namely $\Delta r = v_0 \Delta t$, where v_0 is the local mean speed averaged within the structure. We find that for the current sheet observed by PSP, the width is ~47 km, while for the one observed by Solar Orbiter, the width is ~692 km. To make a quantitative comparison, we normalize Δr to the characteristic proton scales, estimated locally in each structure, and we observe that the width of both current sheets is comparable. In particular, $\Delta r_{\rm PSP} \sim 5.3\lambda_i$ or $\sim 5.9\rho_i$, while $\Delta r_{\rm SolO} \sim 7.7\lambda_i$ or $\sim 6.5\rho_i$.

In Fig. 10 we present two examples of a vortex-like structure, such as an Alfvén vortex (Alexandrova et al. 2006; Lion et al. 2016; Roberts et al. 2016; Perrone et al. 2017, 2020; Wang et al. 2019). In both events, the fluctuations, characterized by $\lambda_{\rm min} \ll \lambda_{\rm int} < \lambda_{\rm max}$, are well localized and the main variance is in the plane perpendicular to $\boldsymbol{b}_0$, with very small compressive fluctuations, $\delta b_z \ll \delta b_x, \delta b_y$. Looking in greater detail at the results of the minimum variance analysis, we find that both the maximum and intermediate direction of variations are perpendicular to $\boldsymbol{b}_0$, namely $\theta_{\rm max} \sim 86°$ and $\theta_{\rm int} \sim 81°$ for the structure at 0.1 AU, and $\theta_{\rm max} \sim 85°$ and $\theta_{\rm int} \sim 78°$ for the structure at 0.97 AU. On the other hand, the direction of minimum variance is almost parallel to the local magnetic field, with $\theta_{\rm min} \sim 10°$ and ~13° for the vortex-like structures observed by PSP and Solar Orbiter, respectively. Finally, their characteristic widths are $\Delta r_{\rm PSP} \sim 89$ km $\sim 9.7\lambda_i$ or $\sim 11.7\rho_i$ and $\Delta r_{\rm SolO} \sim 2106$ km $\sim 24.6\lambda_i$ or $\sim 19.2\rho_i$, suggesting that, during the radial expansion of the wind, the original vortices could merge and generate larger vortices. Such a mechanism of nonlinear interaction among vortices, which are not static structures, has usually been observed in numerical simulations of turbulent solar wind (see e.g., Servidio et al. 2012, 2015; Perrone et al. 2013). However, for the sake of completeness, we have to add that the differences in the size of the vortex-like structures observed by PSP and Solar Orbiter could be also related to the anisotropy in size of the

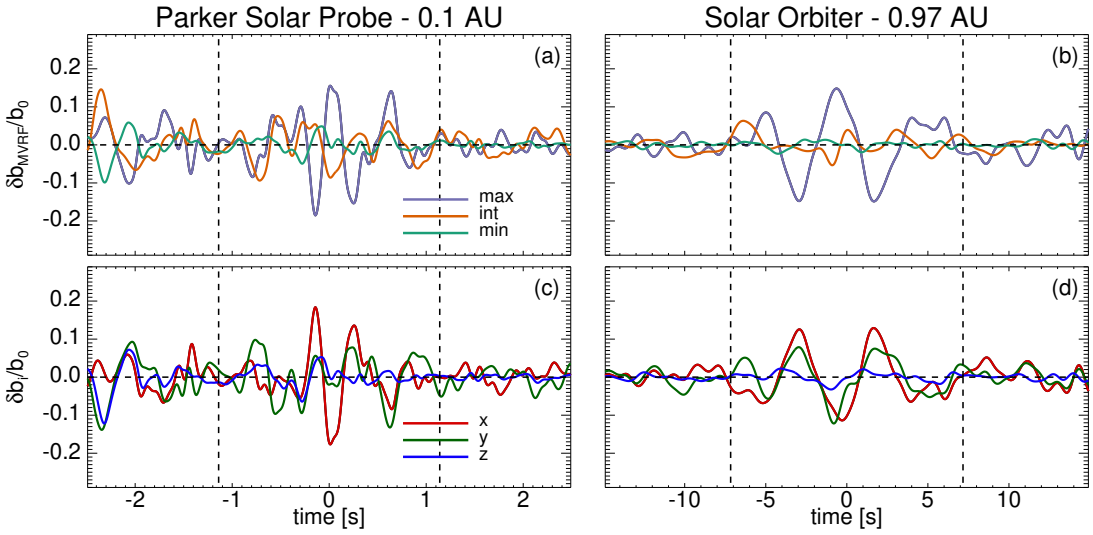

Fig. 10. Example of two vortex-like structures observed at 0.1 AU (*left column*), and at 0.97 AU (*right column*), centered at 02:58:29.55 UT on 28 September and at 00:54:54.34 UT on 25 September, respectively. The panels are the same as those in Fig. 9.

vortices in different directions, and/or how the spacecraft trajectory cuts them.

4. Summary

We have studied the radial evolution in the inner heliosphere, from 0.1 to 1 AU, of a recurrent stream of solar wind coming from the same solar source, namely a coronal hole, by means of combined observations by Solar Orbiter and Parker Solar Probe. This plasma has been observed for the first time at 0.89 AU and, after about 27 days (a solar rotation), at 0.97 AU by Solar Orbiter. Then, at 0.1 AU, PSP was connected to the same coronal hole, allowing, for the first time, a privileged point of observation of this recurrent stream very close to the Sun.

The three intervals are characterized by a nearly constant magnitude of the magnetic field, proton density, speed, and temperature, even if at 0.1 AU these proton quantities show stronger fluctuations. These large fluctuations are related to the presence of spikes in the speed profile and are linked to the switchbacks in the magnetic field radial component. Moreover, in the three intervals, we found a clear correlation between the components of the magnetic and velocity fields, which, in addition to a low compressibility, suggests a high Alfvénicity in these periods.

The study of the radial evolution of the large-scale properties of the recurrent stream, confirming previous findings, showed that the proton density decreases slightly more slowly than expected for a stationary radially expanding plasma, due to the possible presence of secondary proton beams in the velocity distribution function. Furthermore, the radial trend for the proton temperature suggests that some mechanisms of heating are at work locally. Finally, supported by the high Alfvénicity of the intervals, for the magnetic field, we found a deviation from the Parker prediction. Indeed, since the Alfvénic fluctuations are preferentially perpendicular to the ambient magnetic field, they force the radial component to decrease, while they tend to increase the transversal components (Matteini et al. 2015). Therefore, close to the Sun where the Alfvénic fluctuations are stronger, the radial component of the magnetic field should be smaller than expected from the Parker model, while the tangential component should be larger. According to our results, in agreement with Bavassano et al. (1982b), the radial trend of Alfvénic fluctuations is faster than the radial expansion of the wind; and thus its contribution is stronger close to the Sun than at 1 AU, confirming the results of our analysis.

The study of the spectral properties of the three intervals exhibits, as expected, a decrease in the power level during the expansion of the solar wind plasma. Moreover, we found that each period is characterized, in the inertial range, by a power-law between the Kolmogorov spectrum and the Kraichnan scaling. While the velocity spectral index remains quite close to the Iroshnikov-Kraichnan scaling at all the radial distances, the spectral index of the magnetic field fluctuations decreases in absolute value as the radial distance increases from 0.1 to 0.97 AU. The same behavior for the magnetic field fluctuations has been observed in the dissipative range, though with a steeper power-law. This variation seems to be consistent with the different turbulence observed by the spacecraft. Indeed, PSP sampled a more parallel turbulence, since $\cos\theta_{BV} \sim -1$, while Solar Orbiter measured a more perpendicular turbulence.

Focusing on the magnetic field fluctuations, we observed a high level of intermittency in the recurrent fast stream, related to the presence of coherent magnetic events, which decreases as the distance from the Sun increases. Indeed, we found that magnetic field fluctuations around proton scales are characterized by the presence of no compressive coherent structures (Perrone et al. 2016, 2017, 2020), with a bigger number of events detected by PSP close to the Sun with respect to the interval observed by Solar Orbiter at about 1 AU. This difference in the occurrence is expected, due to the different time length of the two considered intervals and to the different characteristic proton scales at those radial distances. These events have a low level of compressibility, are well-localized in space, and have regular profiles. Using an automated method for the selection, they have been found to be current sheets and vortex-like structures, mostly perpendicular to the mean field direction. They have also been found to be present in the plasma in a great number, and thus it would be pivotal to investigate their role in plasma heating by means of the particle distribution functions. This will be deferred to an upcoming study.

To fully characterize the solar wind plasma evolution during its trip from the Sun to the Earth, more observations similar to those used for the present study are required, namely to follow the plasma coming from the same source on the Sun in the

inner heliosphere. Tracing a recurrent stream with more observational points at different radial distances, covering the entire inner heliosphere, is of extreme importance. In this respect, several space missions should be considered, and this is the perfect time for this kind of investigation since in the last few years, a few new missions have been launched to investigate the regions close to the Sun, namely PSP, Solar Orbiter, and BepiColombo. The latter is dedicated to Mercury science, but it also spends a lot of time in the interplanetary medium. For solar wind physics, this is a real golden era.

Acknowledgements. The authors would like to acknowledge the International Space Science Institute (ISSI) for its support of the team 'Unravelling solar wind microphysics in the inner heliosphere' dedicated in part to the analysis of Solar Orbiter data. D.P. would like to acknowledge GL for her constant presence during this work. R.L. was supported by an Imperial College President's Scholarship. S.T.R. acknowledges support of the Ministry of Science and Innovation of Spain (grant PID2020-112805GA-I00). J.E.S. is supported by the Royal Society University Research Fellowship URF/R1/201286.

References

Alexandrova, O., Mangeney, A., Maksimovic, M., et al. 2006, J. Geophys. Res., 111, A12208
Alexandrova, O., Chen, C. H. K., Sorriso-Valvo, L., Horbury, T. S., & Bale, S. D. 2013, Space Sci. Rev., 178, 101
Bale, S. D., Kellogg, P. J., Mozer, F. S., Horbury, T. S., & Reme, H. 2005, Phys. Rev. Lett., 94, 215002
Bale, S. D., Goetz, K., Harvey, P. R., et al. 2016, Space Sci. Rev., 204, 49
Bale, S. D., Badman, S. T., Bonnell, J. W., et al. 2019, Nature, 576, 237
Bavassano, B., Dobrowolny, M., Mariani, F., & Ness, N. F. 1981, J. Geophys. Res., 86, 1271
Bavassano, B., Dobrowolny, M., Fanfoni, G., Mariani, F., & Ness, N. F. 1982a, Solar Phys., 78, 373
Bavassano, B., Dobrowolny, M., Mariani, F., & Ness, N. F. 1982b, J. Geophys. Res., 87, 3617
Belcher, J. W., & Davis, L., Jr. 1971, J. Geophys. Res., 76, 3534
Bruno, R., & Bavassano, B. 1987, Ann. Geophys., 5, 265
Bruno, R., & Carbone, V. 2013, Liv. Rev. Sol. Phys., 10, 2
Bruno, R., & Trenchi, L. 2014, ApJ, 787, L24
Bruno, R., Bavassano, B., & Villante, U. 1985, J. Geophys. Res., 90, 4373
Bruno, R., Carbone, V., Veltri, P., Pietropaolo, E., & Bavassano, B. 2001, Planet. Space Sci., 49, 1201
Bruno, R., Carbone, V., Sorriso-Valvo, L., & Bavassano, B. 2003, J. Geophys. Res., 108, 1130
Bruno, R., Trenchi, L., & Telloni, D. 2014a, ApJ, 793, L15
Bruno, R., Telloni, D., Primavera, L., et al. 2014b, ApJ, 786, 53
Camporeale, E., Carè, A., & Borovsky, J. E. 2017, J. Geophys. Res., 122, 10910
Chen, C. H. K., Bale, S. D., Bonnell, J. W., et al. 2020, ApJS, 246, 53
Coleman, P. J., Jr. 1968, ApJ, 153, 371
D'Amicis, R., Bruno, R., Pallocchia, G., et al. 2010, ApJ, 717, 474
D'Amicis, R., & Bruno, R. 2015, ApJ, 805, 84
D'Amicis, R., Bruno, R., Panasenco, O., et al. 2021a, A&A, 656, A21
D'Amicis, R., Perrone, D., Bruno, R., & Velli, M. 2021b, J. Geophys. Res., 126, e28996
Duan, D., Browen, T. A., Chen, C. H. K., et al. 2020, ApJS, 246, 55
Dudok de Wit, T., Krasnoselskikh, V. V., Bale, S. D., et al. 2020, ApJS, 246, 39
Farge, M. 1992, Ann. Rev. Fluid Mech., 24, 395
Fox, N. J., Velli, M., Bale, S. D., et al. 2016, Space Sci. Rev., 204, 7
Frisch, U. 1995, Turbulence. The Legacy of A. N. Kolmogorov (Cambridge: Cambridge University Press, UK)
Goldreich, P., & Sridhar, S. 1995, ApJ, 438, 763
Harvey, J. W., Hill, F., Hubbard, R. P., et al. 1996, Science, 272, 1284
He, J., Tu, C., Marsch, E., & Yao, S. 2012, ApJ, 745, L8
He, J., Tu, C., Marsch, E., Bourouaine, S., & Pei, Z. 2013, ApJ, 773, 72
Hellinger, P., Matteini, L., Stverák, S., Trávnícek, P. M., & Marsch, E. 2011, J. Geophys. Res., 116, A09105
Hellinger, P., Trávnícek, P. M., Stverák, S., Matteini, L., & Velli, M. 2013, J. Geophys. Res., 118, 1351
Horbury, T. S., Forman, M., & Oughton, S. 2008, Phys. Rev. Lett., 101, 175005
Horbury, T. S., Matteini, L., & Stansby, D. 2018, MNRAS, 478, 1980
Horbury, T. S., O'Brien, H., Carrasco Blazquez, I., et al. 2020a, A&A, 642, A9
Horbury, T. S., Woolley, T., Laker, R., et al. 2020b, ApJS, 246, 45
Jokipii, J. R., & Kóta, J. 1989, Geophys. Res. Lett., 16, 1
Kasper, J. C., Abiad, R., Austin, G., et al. 2016, Space Sci. Rev., 204, 131
Kasper, J. C., Bale, S. D., Belcher, J. W., et al. 2019, Nature, 576, 228
Kiyani, K. H., Chapman, S. C., Khotyaintsev, Yu. V., Dunlop, M. W., & Sahraoui, F. 2009, Phys. Rev. Lett., 103, 075006
Kolmogorov, A. 1941, Dokl. Akad. Nauk SSSR, 30, 9
Kraichnan, R. H. 1965, Phys. Fluids, 8, 1385
Lavraud, B., Kieokaew, R., Fargette, N., et al. 2021, A&A, 656, A37
Leamon, R. J., Matthaeus, W. H., Smith, C. W., & Wong, H. K. 1998, ApJ, 507, L181
Lemen, J. R., Title, A. M., Akin, D. J., et al. 2012, Sol. Phys., 275, 17
Lion, S., Alexandrova, O., & Zaslavsky, A. 2016, ApJ, 824, 47
Livi, R., Larson, D. E., Kasper, J. C., et al. 2021, ApJ, submitted
Louarn, P., Fedorov, A., Prech, L., et al. 2021, A&A, 656, A36
Mariani, F., Villante, U., Bruno, R., Bavassano, B., & Ness, N. F. 1979, Sol. Phys., 63, 411
Marsch, E. 2006, Liv. Rev. Sol. Phys., 3, 1
Marsch, E., & Tu, C. Y. 1997, Nonlinear Proc. Geophys., 4, 101
Marsch, E., Muhlhauser, K.-H., Schwenn, R., et al. 1982, J. Geophys. Res., 87, 52
Matteini, L., Horbury, T. S., Pantellini, F., Velli, M., & Schwartz, S. J. 2015, ApJ, 802, 11
Moncuquet, M., Meyer-Vernet, N., Issautier, K., et al. 2020, ApJS, 246, 44
Müller, D., St. Cyr, O. C., Zouganelis, I., et al. 2020, A&A, 642, A1
Neugebauer, M., Forsyth, R. J., Galvin, A. B., et al. 1998, J. Geophys. Res., 103, 14587
Owen, C. J., Bruno, R., Livi, S., et al. 2020, A&A, 642, A16
Owen, C. J., Foster, A. C., Bruno, R., et al. 2021, A&A, 656, L8
Parker, E. N. 1958, ApJ, 128, 664
Perrone, D., Valentini, F., Servidio, S., Dalena, S., & Veltri, P. 2013, ApJ, 762, 99
Perrone, D., Alexandrova, O., Mangeney, A., et al. 2016, ApJ, 826, 196
Perrone, D., Alexandrova, O., Roberts, O. W., et al. 2017, ApJ, 849, 49
Perrone, D., Stansby, D., Horbury, T. S., & Matteini, L. 2019a, MNRAS, 483, 3730
Perrone, D., Stansby, D., Horbury, T. S., & Matteini, L. 2019b, MNRAS, 488, 2380
Perrone, D., Bruno, R., D'Amicis, R., et al. 2020, ApJ, 905, 142
Pesnell, W. D., Thompson, B. J., & Chamberlin, P. C. 2012, Sol. Phys., 275, 3
Podesta, J. J., Roberts, D. A., & Goldstein, M. L. 2006, J. Geophys. Res., 111, A10109
Podesta, J. J., Roberts, D. A., & Goldstein, M. L. 2007, ApJ, 664, 543
Ragot, B. R. 2006, ApJ, 651, 1209
Roberts, D. A. 2010, J. Geophys. Res., 105, A12101
Roberts, D. A., Goldstein, M. L., Klein, L. W., & Matthaeus, W. H. 1987, J. Geophys. Res., 92, 12023
Roberts, O. W., Li, X., Alexandrova, O., & Li, B. 2016, J. Geophys. Res., 121, 3870
Sahraoui, F., Goldstein, M. L., Robert, P., & Khotyaintsev, Yu. V. 2009, Phys. Rev. Lett., 102, 231102
Sahraoui, F., Goldstein, M. L., Belmont, G., Canu, P., & Rezeau, L. 2010, Phys. Rev. Lett., 105, 131101
Salem, C., Mangeney, A., Bale, S. D., & Veltri, P. 2009, ApJ, 702, 537
Schwartz, S. J., & Marsch, E. 1983, J. Geophys. Res., 88, 9919
Schwenn, R. 1983, NASA Conf. Publ., 2280, 489
Servidio, S., Valentini, F., Califano, F., & Veltri, P. 2012, Phys. Rev. Lett., 108, 045001
Servidio, S., Valentini, F., Perrone, D., et al. 2015, J. Plasma Phys., 81, 325810107
Shi, C., Velli, M., Panasenco, O., et al. 2021, A&A, 650, A21
Sonnerup, B., & Scheible, M. 1998, Analysis Methods for Multi-Spacecraft Data (The Netherlands: ESA Publ. Div.)
Sorriso-Valvo, L., Carbone, V., Veltri, P., Consolini, G., & Bruno, R. 1999, Geophys. Res. Lett., 26, 1801
Sorriso-Valvo, L., Catapano, F., Retinò, A., et al. 2019, Phys. Rev. Lett., 122, 035102
Stansby, D. 2017, https://doi.org/10.5281/zenodo.1009506
Stansby, D., Horbury, T. S., & Matteini, L. 2018, MNRAS, 482, 1706
Stansby, D., Yeates, A., & Badman, S. T. 2020, J. Open Sour. Softw., 5, 2732
Telloni, D., Bruno, R., & Trenchi, L. 2015, ApJ, 805, 46
Telloni, D., Sorriso-Valvo, L., Woodham, L. D., et al. 2021, ApJ, 912, L21
Torrence, C., & Compo, G. P. 1998, Bull. Am. Meteorol. Soc., 79, 61
Tu, C.-Y., & Marsch, E. 1995, Space. Sci. Rev., 73, 1
Verscharen, D., Klein, K. G., & Maruca, B. A. 2019, Liv. Rev. Sol. Phys., 16, 5
von Papen, M., & Saur, J. 2015, ApJ, 806, 116
Wang, T., Alexandrova, O., Perrone, D., et al. 2019, ApJ, 871, L22
Woodham, L. D., Horbury, T. S., Matteini, L., et al. 2021, A&A, 650, L1
Wu, P., Perri, S., Osman, K., et al. 2013, ApJ, 763, L30
Yordanova, E., Perri, S., Sorriso-Valvo, L., & Carbone, V. 2015, Europhys. Lett., 110, 19001